Non-equilibrium Spin Dynamics of the Frustrated Trication Spinel $ZnMnCoO_4$ in the Hierarchical Free-energy Framework

Mouli Roy-Chowdhury,[1] Tapati Sarkar,[2] Bruno Weise,[3] Eun Sang Choi,[4] Zhenchao Wen,[5] and Subhash Thota[1,*]

[1] *Department of Physics, Indian Institute of Technology Guwahati-781039, Assam, India.*
[2] *Department of Materials Science and Engineering, Uppsala University, SE-75103, Sweden.*
[3] *Leibniz-IFW Dresden, Institute for Complex Materials, D-01069 Dresden, Germany.*
[4] *National High Magnetic Field Laboratory, Tallahassee, FL 32310-3706, United States of America.*
[5] *National Institute for Materials Science (NIMS), 1-2-1 Sengen, Tsukuba 305-0047, Japan.*

(Dated: December 18, 2024)

Short-range spin correlations, memory and rejuvenation effects have been reported in the trication oxispinel $ZnMnCoO_4$ whose low-temperature spin dynamics, triggered by magnetic frustration ($f_r \sim 6$), could be better explained by the 'phenomenological' hierarchical spin-glass model than the short-range droplet theory. Accordingly, the aging mechanism of the system had an asymmetric memory response to the positive and negative thermal cycles within the cluster-glass state ($T < 32.6$ K), demonstrated a hierarchical organization of the phase space where its metastable energy states undergo continuous splitting with decreasing temperature. An attempt to reproduce the time evolution of the isothermal remanent magnetization in the system led to an investigation of various relaxation models featuring semi-logarithmic, algebraic, fractional or stretched-exponential tails. Nevertheless, Weron's probabilistic relaxation model (here, the fractal character $\beta \sim 0.4$, the hierarchical constraint $k > 0$, and the order parameter $q(T \sim 0.12T_{SG}) = 1.88$) based on a purely stochastic approach, was best suited for understanding the slow spin dynamics of the cluster-glass phase in the entire temporal range. A comprehensive picture of the magnetic phase map was developed for the system, aided by magnetometry techniques and heat-capacity studies.

I. INTRODUCTION

Mixed transition-metal (TM) spinels represent real correlated-electron systems which often display unconventional phenomena due to the interplay of spin, lattice, and orbital degrees of freedom [1]. The multi-component spinel oxide lattice has two cation sites, A and B present in 1:2 ratio along with 4 anion sites per formula unit (f.u.). In contrast to the isolated AO_4 tetrahedra, B cations form edge-sharing octahedra in coordination with the oxygen anions (BO_6). The electronic configurations in such TM spinels and their cationic distribution are strongly affected by the electrostatic interactions between the crystal field (CF) of ligands and the outer d-orbitals in TM. Among all the intriguing problems discussed in the backdrop of TM spinels, the emergence of frustrated magnetism seems to have earned widespread attention in recent years.

The origin of frustration in spinels may be attributed to one or more of the reasons listed here: (*i*) competing nearest neighbour (NN) and next neighbour exchange (NNN) interactions, (*ii*) unique underlying lattice geometries such as the 2D Kagome and Triangular planes or the 3D pyrochlore structure, (*iii*) magnetic and/or occupational disorder, and (*iv*) competing ferromagnetic (FM) and antiferromagnetic (AFM) interactions [2]. Such effects may culminate into a non-trivial, non-ergodic state known as the spin-glass (SG) where history-dependent spin dynamics indicative of non-equilibrium behavior dominates [3]. Additionally, the SG model has proved to be a popular prototype of complex correlated systems in the last few decades, with applications beyond its original scope, such as in combinatorial optimization, neurology, information theory, and so on [4]. The SG state, also styled as the "cooperative paramagnet", predominantly possesses short-range magnetic correlations and a macroscopic ground-state degeneracy. Such 'glassy' phase is further characterized by aging effect, non-exponential response to external perturbations, slow dynamics, non-Arrhenius temperature dependence of relaxation time scales, exchange bias, etc. [3]. Despite numerous experimental and theoretical studies, the magnetic ground state and relaxation dynamics in SG systems still deserve further clarity.

Magnetically diluted solid solutions with the spinel structure in which magnetic moments only occupy the octahedral B-sites, display magnetic frustration. When the NN magnetic coupling J_{BB} is AFM in nature while A-site cations are diamagnetic, the frustration in the system becomes strong enough to impede the onset of long-range order down to low temperatures and may lead to the appearance of the SG phase. In this context, our study is based on the experimental investigation of $ZnMnCoO_4$ which is governed by magnetic dilution effects, frustration and dominant antiferromagnetic NN exchanges. From henceforth, $ZnMnCoO_4$ will be referred to by its shorthand, ZMCO for brevity. The introduction of Co^{3+} at half of the octahedral Mn^{3+} sites in tetragonal $ZnMn_2O_4$ alters the parent crystal symmetry [tetragonal ($I41/amd$)] while inducing disorder in the already frustrated pyrochlore-like B sublattice. This substitution results in ZMCO which is isostructural to the cubic (Fd-$3m$) spinel Co_3O_4. Existing reports on $ZnMn_2O_4$ confirm

* Corresponding author: subhasht@iitg.ac.in

an AFM order although its spin-structure and ordering temperature is still under debate due to conflicting studies [5, 6]. On the other hand, Cossee observed a weak paramagnetism in the other end compound, $ZnCo_2O_4$ although Co^{3+} cations are diamagnetic in most octahedral Co complexes [7]. Hence, the intermediary ZMCO experiences magnetic dilution effects due to the incorporation of low-spin (S = 0) octahedral Co^{3+} ions under the influence of a large crystal-field splitting between t_{2g} and e_g levels [8, 9]. From the viewpoint of technological advances, ZMCO has been investigated as a potential candidate in Zn-based battery systems which seem to be more advantageous over their lithium counterparts [10, 11]. Furthermore, the incorporation of cobalt into the $ZnMn_2O_4$ lattice was reported to improve the spin compatibility and durability of the compound, thus, improving their catalytic performance in oxygen evolution reactions within alkaline media [12]. All these factors render ZMCO fundamentally interesting to investigate. Our experimental study employs the opportunity to study the effects of dilute magnetic interactions with a special focus on the structural, electronic and magnetic properties of the normal (2-3) cubic spinel ZMCO. We unveiled a 'hierarchical' SG ground state, characterized by magnetic spin clusters instead of individual spins along with only short-range magnetic order throughout the temperature scale. The system demonstrated robust memory and rejuvenation effects, non-trivial temperature and time evolution of isothermal remanent magnetization which were modelled using well-known relaxation models [13–15]. Details of our experimental procedures, results, and their subsequent interpretation are presented below.

II. EXPERIMENTAL METHODOLOGY

A. Material Synthesis:

Polycrystalline bulk sample of tricationic ZMCO was synthesized using the conventional solid-state reaction method under high-temperature and ambient pressure conditions. Stoichiometric proportions of binary TM oxides of Zn, Mn and Co were ground together into a uniform mixture. Polyvinyl alcohol was mixed with the homogenized powder as a binder before it was pressed into pellets of 13 mm diameter using a hydraulic press (Force $\sim$ 40 kN). The pellets were sintered in an alumina crucible at a constant temperature of 1474 K in air for 8 h at a rising rate of 278 K/min, and then allowed to cool down to room temperature naturally in air.

B. Measurement Techniques:

The phase purity and crystal structure of the synthesized product were confirmed from the powder x-ray diffraction (PXRD) patterns obtained in $\theta - 2\theta$ geometry at room temperature and atmospheric pressure using a RIGAKU x-ray diffractometer (Model: TTRAX III) with Cu-Kα radiation (wavelength λ = 1.5406 Å, Power = 18 kW). The PXRD spectra was recorded at a slow scan rate of 2°/min from $2\theta = 10°$ to 80° with step size $\sim 0.02°$. Ex-situ x-ray photoelectron spectroscopy (XPS) was performed on the sample to determine its electronic structure by employing an automated ultra-high vacuum XPS instrument from M/s Physical Electronics, USA (Model: PHI 5000 versa probe III). The magnetic nature of ZMCO was probed by *ac* and DC magnetometry along with molar heat capacity measurements. A superconducting quantum interference device based magnetometer (SQUID-MPMS) and a vibrating sample magnetometer based physical property measurement system (PPMS-VSM), both from Quantum Design were used to measure the *ac* and DC magnetization of ZMCO. A PPMS from Quantum Design was also employed to perform temperature-dependent specific heat capacity measurements on the ZMCO sample for both $H_{DC} = 0$ and $H_{DC} = 90$ kOe using the heat-pulse calorimetry method involving slope analysis [16].

III. RESULTS AND DISCUSSION

A. Crystal Structure Determination:

The Bragg peaks in the PXRD pattern of ZMCO could all be indexed under a cubic Fd-$3m$ ($F^4_{1/d}\bar{3}_{2/m}O^7_h$; No. 227 according to the International Tables for Crystallography) lattice which is quite typical for spinels [17]. The Rietveld structural refinement (RSR) method was applied on the PXRD pattern using the FULLPROF suite. In FULLPROF, the peaks were fitted by a pseudo-Voigt profile with low values of $\chi^2 = 1.6$ and Bragg R-factor = 3.8. The acquired RSR data is represented in Fig. S1(a) given in the supplemental information (SI) file [18]. The VESTA software generated a schematic illustration of the ZMCO unit-cell with 137 atoms, 218 bonds and 39 polyhedra from the RSR data (inset of Fig. S1(a)) [18]. The lattice parameters for the system were $a = b = c = 8.3739(5)$ Å with a unit-cell volume ~ 587.2 Å^3. Table SI lists the crystallographic parameters such as bond lengths, bond angles, site occupancies, Wyckoff positions, and point symmetries from the VESTA visualization. The tetrahedral (Zn) and octahedral (Mn and Co) cations occupied fixed positions on equipoints $8a$ ($\frac{1}{8}, \frac{1}{8}, \frac{1}{8}$) and $16d$ ($\frac{1}{2}, \frac{1}{2}, \frac{1}{2}$), respectively with $\bar{3}m$ as the unit-cell origin. Ideally, the O^{2-} anions in a spinel oxide should be located on equipoint $32e$ (0.2512, 0.2512, 0.2512), however, in reality, their exact positions are determined by the oxygen parameter u. Here, $u = 0.2512(2)$ (0.49% increase) indicates slight anion dilation which accommodates differences in the effective cationic radii, and thus, impacts bond lengths and polyhedral volumes. The slight increment in u for ZMCO indicates an enhanced tetrahedron size. Consequently, the octahedra shrinks and exhibits a reduced symmetry of $\bar{3}m$ instead of $m\bar{3}m$

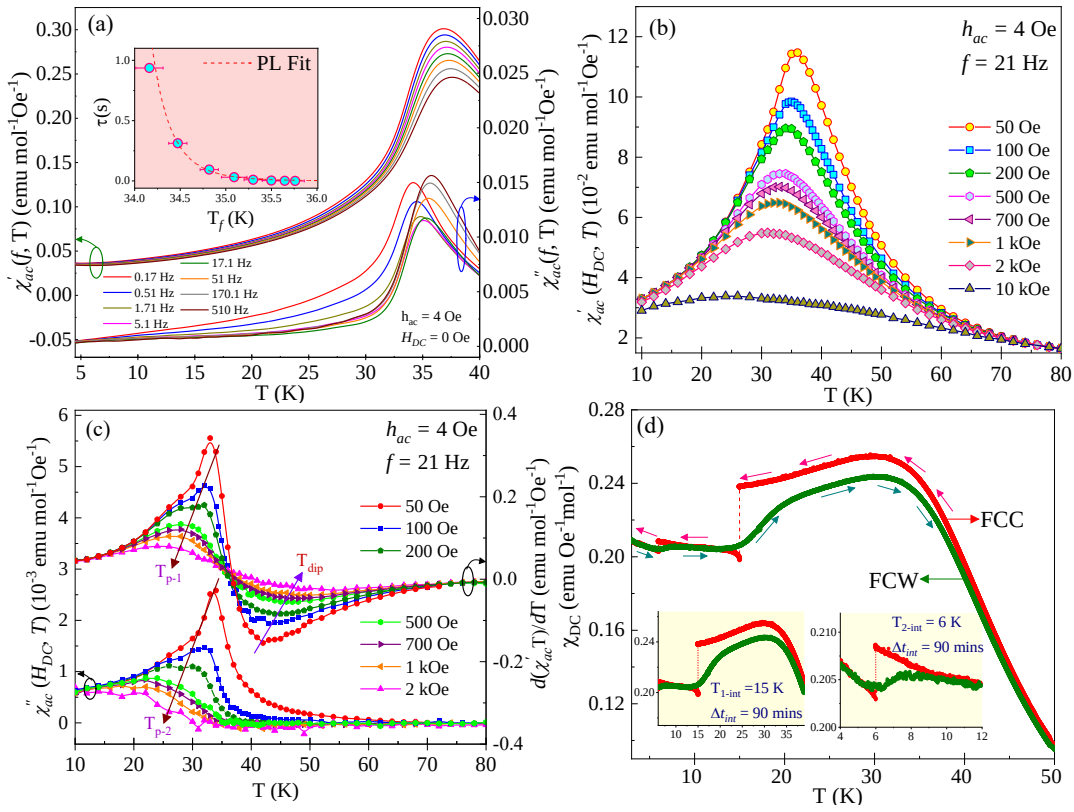

FIG. 1. (a) Temperature variation of the real $\chi'_{ac}(f,T)$ (left-hand axis) and imaginary $\chi''_{ac}(f,T)$ (right-hand axis) components of the *ac*-susceptibility of ZMCO measured at various frequencies between 0.17 Hz to 510 Hz. The measurements were recorded under warming conditions using an *ac* field of peak-to-peak amplitude $h_{ac} = 4$ Oe and no DC bias. The inset contains the PL fit to the experimental data and an error bar is provided for each data point. (b) Temperature variation of $\chi'_{ac}(H_{DC},T)$ for ZMCO measured at constant $f = 21$ Hz and $h_{ac} = 4$ Oe under superposed DC bias fields listed in the figure, are shown here. (c) Left-hand scale: Plots of $\chi''_{ac}(H_{DC},T)$ vs. T for ZMCO measured at $f = 21$ Hz and $h_{ac} = 4$ Oe in the presence of superposed DC bias fields; Right-hand scale: The $\mathrm{d}(\chi'_{ac}(H_{DC},T)/\mathrm{dT}$ vs. T curves computed from 3(b). The arrows illustrate the direction of peak shift with increasing bias fields. (d) This plot depicts the memory of the system by measuring its magnetization curve as a function of temperature under FC protocol in a manner described within the text. The insets show the zoomed portions of the curve at two different halt temperatures, 15K and 6K where the system was allowed to wait and age for 90 minutes.

in case of a regular octahedra [19]. Fig. S1(b) depicts the network of corner-sharing *B*-tetrahedra forming a pyrochlore sublattice with inherent geometrical frustration [18]. The Zn-tetrahedra engaged in no edge-sharing while the $[Mn/Co]O_6$ octahedra shared six edges with adjacent octahedra and the remaining six edges surrounded vacant lattice sites with point symmetry 16*c* [19, 20]. Table SII contains the experimental and theoretical lattice distances of closest approach between the constituent ions which depend only on *a* and *u*. As expected for a cubic spinel lattice, *B*-*B* lattice separations for ZMCO were the shortest among all cationic distances.

B. Electronic structure:

The XPS studies on ZMCO yielded the core level spectra of O-1*s*, Zn-2*p*, Co-2*p*, and Mn-2*p* as a function of binding energy (B.E. in eV units). The photoelectron emission lines for all four constituents were corrected using adventitious carbon as an internal reference, C-1*s* ($E_C = 284.8$ eV). Mathematical fits to a Tougaard function was used for background correction while each spectrum was deconvoluted into Gaussian-Lorentzian peaks using the XPSPEAK41 software. Fig. S1(c) graphically represents the O-1*s* photoemission spectrum which was deconvoluted into an intense peak at 529.5 eV due to metal-oxygen bonding in the lattice and a subdued peak around 531.18 eV attributed to adsorbed surface oxygen [18, 21, 22]. The core-level Zn-2*p* spectrum (Fig. S1(d))

was resolved into two peaks centered at 1020.4 eV (Zn-$2p_{3/2}$) and 1043.5 eV (Zn-$2p_{1/2}$), respectively [18]. The resultant spin-orbit energy gap $\Delta E_{Zn} \sim 23.1$ eV confirmed the divalency of the tetrahedral Zn cations [23]. Figure S1(e) displays two prominent peaks at 779.9 eV and 795.2 eV in the Co-2p spectra which are respectively attributed to Co-$2p_{3/2}$ and Co-$2p_{1/2}$ [18]. The energy difference between these electronic states ΔE_{Co} ($2p_{1/2}$ - $2p_{3/2}$) = 15.3 eV signifies the presence of Co^{3+} in ZMCO [24, 25]. The main line for Co-$2p_{3/2}$ and Co-$2p_{1/2}$ are accompanied by very weak satellite structures around 786 eV and 804 eV, respectively, on the B.E. axis. These satellite peaks often arise during photoemission either due to 'shake-up' processes or charge transfer between Co ($3d^6$) valence shell and filled 2p orbitals of oxygen ligands [25, 26]. Finally, the Mn-2p photoelectron spectrum (Fig. S1(f)) could be resolved into 2 main peaks located at 641.4 eV (Mn-$2p_{3/2}$) and 653.2 eV (Mn-$2p_{1/2}$), and a very weak satellite around 644.1 eV [18]. This confirmed the oxidation state of Mn as Mn^{3+} with $\Delta E_{Mn} = 11.8$ eV [22]. The slightly higher value of ΔE_{Mn} observed for Mn^{3+} in ZMCO than that reported for $MnCo_2O_4$ ($\sim$ 11.21 eV) could possibly result from screening and CF effects due to Zn incorporation in the lattice [24, 27]. Slight shifts in the peak positions are common in complex oxides due to different local environments at different lattice sites. Thus, we concluded that the electronic structure of ZMCO was $(Zn^{2+})_{8a}[Co^{3+}\ Mn^{3+}]_{16d}\ [O_4{}^{2-}]_{32e}$.

C. Frequency and Bias Field dependence of *ac*-susceptibility:

Fig. 1(a) presents the temperature dependence of both components of *ac*-susceptibility, $\chi'_{ac}(f,T)$ (real) and $\chi''_{ac}(f,T)$ (imaginary) for ZMCO in the frequency range, 0.17 Hz $\leq f \leq$ 510 Hz under a fixed excitation field h_{ac} = 4 Oe and zero DC biasing field. Appearance of rounded peaks with frequency dependent amplitude and position, in both *ac*-susceptibility curves could be attributed to an energy dissipation process associated with domain dynamics. The peak amplitude in $\chi'_{ac}(f,T)$ vs. T decreased with increasing f, while for $\chi''_{ac}(f,T)$ vs. T, the amplitude first decreased for all frequencies up to 5.1 Hz, and then increased upon further increase in f. Such unconventional effect of frequency on the amplitude in $\chi''_{ac}(f,T)$ has been previously observed in other cluster SG systems [28, 29]. Moreover, in both cases, the maxima gradually shift towards higher temperatures with an increase in f attesting to a SG-like transition. The relative shift of the maxima in (δT_f) per decade of frequency is quantified by the Mydosh parameter Ω_M. Ω_M, a popular SG classification criterion, provides a measure of the strength of intercluster interactions via their frequency response. In case of weak interactions, the frequency dispersion is stronger while it becomes almost negligible for strong spin-spin interactions, such as in normal magnets. Quantitatively, $\Omega_M = [\frac{T_f(f_{high})}{T_f(f_{low})}\text{-}1][\log_{10}(\frac{f_{high}}{f_{low}})]^{-1}$, where $T_f(f_{high})$ and $T_f(f_{low})$ are the freezing temperatures experimentally observed at excitation frequencies, f_{high} and f_{low}, respectively [23, 30]. $\Omega_M = 0.013$ for ZMCO lies in the cluster SG range, like $ZnTiCoO_4$ ($\Omega_M = 0.026$), $Cr_{0.5}Fe_{0.5}Ga$ ($\Omega_M = 0.017$), Co_2RuO_4 ($\Omega_M = 0.01$), e.t.c. [23, 30, 31]. Typically, Ω_M is an order of magnitude less for canonical SG systems such as AuMn ($\Omega_M = 0.0045$), CuMn (Ω_M = 0.005) and an order of magnitude higher for superparamagnets like α-[$Ho_2O_3(B_2O_3)$] ($\Omega_M = 0.28$) [3, 32]. The inset in Fig. 1(a) shows the best fit of relaxation time τ (= $1/2\pi f$) vs. spin-freezing temperature T_f data to the dynamical scaling model known as the Power Law or PL: $\tau = \tau_0^*[(T_f/T_{SG}-1)]^{-z\nu}$, which describes the critical slowing down behavior on approaching the SG transition temperature, T_{SG} [3, 23, 31]. In the above equation, τ_0^* is the characteristic fluctuation time scale which is related to the correlation length ζ as $\tau \sim \zeta^z$, z being the dynamic critical exponent. Further, T_{SG} is the static freezing temperature as $f \to 0$, and ν represents the critical exponent of ζ (= $[T_f/T_{SG}-1]^{-\nu}$). The best fit to PL resulted in

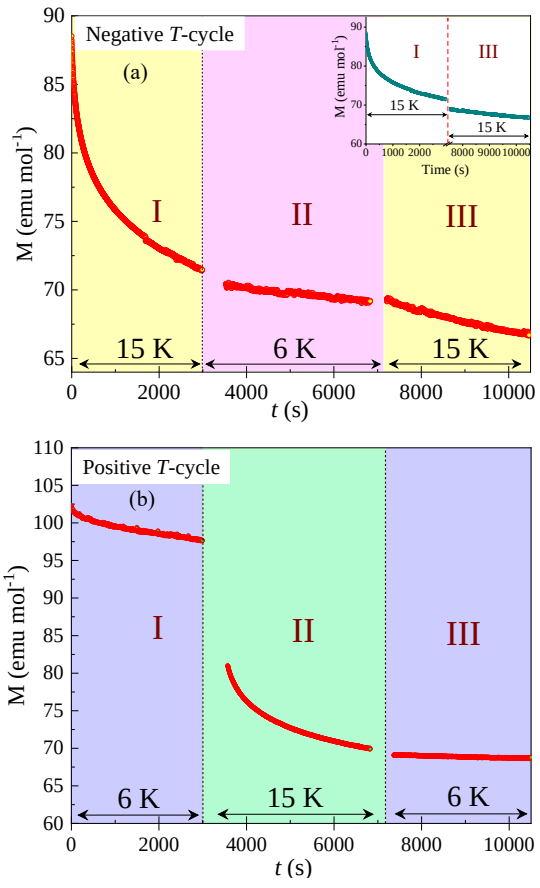

FIG. 2. Asymmetrical memory response of ZMCO when subjected to (a) negative and (b) positive temperature (T) cycles which highlights the hierarchical organization of the energy states of the system within the SG phase. Details of the measurement and interpretation of such behavior in ZMCO are included in the main text.

(*i*) $T_{SG} = 32.6 \pm 0.07$ K, (*ii*) $\tau_0^* = 1.14 \pm 0.025 \times 10^{-10}$ s, and (*iii*) $z\nu = 7.5 \pm 0.16$. Typically, the magnitude of $z\nu$ falls in the range 4 - 12 for SG, the value of τ_0^* lies between $\sim 10^{-12}$ - 10^{-13}s for canonical SG and 10^{-7} - 10^{-10}s for cluster SG systems [3, 23, 28, 30, 31]. The large value of τ_0^*, $\sim 10^2 - 10^3$ times larger than canonical SG systems with shorter spin-flip times, signifies slower spin dynamics in ZMCO due to the presence of larger magnetic entities such as interacting spin clusters rather than individual spins [28, 30, 31]. Thus, we can conclude from the PL analysis that ZMCO exhibits cluster SG behavior.

Temperature ($10 \geq T \geq 80$ K) dependent $\chi'_{ac}(H_{DC}, T)$ and $\chi''_{ac}(H_{DC}, T)$ measurements at a fixed driving frequency of 21 Hz and $h_{ac} = 4$ Oe, superimposed by DC bias fields ranging between 49 Oe and 2100 Oe were used to further probe the cluster SG phase in ZMCO. Fig. 1(b) shows $\chi'_{ac}(H_{DC}, T)$ vs. T curves which exhibit a decrease in the peak temperature along with peak broadening as H_{DC} increased. While in Fig. 1(c), both $\chi''_{ac}(H_{DC}, T)$ vs. T and $d(\chi'_{ac}\mathrm{T})/d\mathrm{T}$ vs. T plots exhibit pronounced peaks T_{P-1} and T_{P-2} respectively, whereas the derivative curve has an additional minima T_{dip}. The visual similarity between the peaks in both the plots of Fig. 1(c) has a theoretical basis since $\chi''_{ac}(H_{DC}, T)$ which peaks at $\omega\tau = 1$ is related to $\chi'_{ac}(H_{DC}, T)$ by the equation: $\chi''_{ac}(H_{DC}, T) \sim [\pi/2ln(f_0/2\pi f_m)]\mathrm{d}(\chi'_{ac}(H_{DC}, T))/\mathrm{dT}$. This feature has also been observed in other systems like α-$Ni(OH)_2$, $ZnTiCoO_4$, etc. [23, 33]. Both T_{P-1} and T_{P-2} exhibited peak-broadening, decreasing amplitudes and a shift in peak position to lower temperatures with an increase in H_{DC} which are hallmark traits of the SG phase. Contrarily, T_{dip} experiences a concomitant increase to higher temperatures as H_{DC} increases, signalling the occurrence of non-SG like behavior in ZMCO just above the SG phase. A non-linear $H_{DC}^{2/3}$ variation of T_{P-1} and T_{P-2} signifies a deviation from the mean-field theory which marks the absence of the de Almeida-Thouless (AT) line. Thus, ZMCO belongs to a different universality class (Fig S2 in SI) [18, 34].

D. Rejuvenation phenomena and magnetic memory effects:

Magnetic memory measurements were performed under the field-cooled (FC) protocol in order to study the broken ergodicity in ZMCO.

1. Temperature variation of interrupted magnetization:

To perform this measurement, a specimen sample of ZMCO was first cooled down from the paramagnetic (PM) state to 3 K in the presence of an applied magnetic field, $H_a = 500$ Oe at a constant cooling rate with wait time interruptions of $\Delta t_{int} = 90$ mins each at $T_{1-int} = 15$ K and $T_{2-int} = 6$ K, both well below T_{SG}. During Δt_{int}, H_a was switched off which allowed the system to undergo relaxation and after each wait, H_a was restored and the FC process was resumed. Fig. 1(d) displays the step-like nature of FC magnetization at 15 K and 6 K and the insets present a zoomed view of the magnetization curves at the halt temperatures. After reaching 3 K, the sample was warmed back to the PM state in the presence of H_a but this time the process remained uninterrupted. This measurement provided experimental evidence of the sample's memory of its measurement history, thus, confirming the existence of a low-temperature SG phase. Further experiments were planned to investigate the nature and directionality of the sample's magnetic memory.

2. Magnetic response to negative thermal (T) cycle:

Another measurement technique was employed to verify the magnetic memory of ZMCO by subjecting the sample to a negative T-cycle under FC conditions. The resulting curve is shown in Fig. 2(a). Here, the sample was first cooled down from the PM state to 15K (well within the SG phase) under $H_a = 500$ Oe. Upon reaching 15 K, H_a was switched off for $\Delta t_1 = 50$ mins during which the magnetization ($M(t)$) curve was recorded as a function of time, while the system was allowed to 'age'. In some SG systems, it is observed that when the system quenched from a temperature above T_{SG} to a wait temperature within the glassy phase, the aging path is "kept in memory" (memory effect) by the system and simultaneously "forgotten" (rejuvenation) upon further cooling [35]. The aged configuration can be recovered upon reheating such systems to the wait temperature, similar to ZMCO during the negative T-cycle. Maintaining the zero-field condition, the sample was further cooled down to 6 K and $M(t)$ was again measured for $\Delta t_2 = 50$ mins. During this step, the curve followed a different path owing to a rearranged spin-configuration on shorter length scales and remained almost constant with t. As a final step, the sample was warmed back to 15 K in the absence of H_a and an exponential time decay of $M(t)$ was once again restored during $\Delta t_3 = 50$ mins. The inset in Fig. 2(a) compares the $M(t)$ data measured during Δt_1 and Δt_3 at 15 K and both seemed to follow a continuous decay path. Hence, when the initial temperature conditions were restored, ZMCO recalled its initial state and cycled back to it despite experiencing intermediary changes. Such a response clearly demonstrated memory effect in ZMCO during negative T-cycle.

3. Magnetic response to positive thermal (T) cycle:

Fig. 2(b) represents the time evolution of magnetization, $M(t)$, for ZMCO under the influence of a positive T-cycle. In this case, the sample was initially cooled down to 6 K in the presence of H_a where $M(t)$ was mea-

sured for $\Delta t_1 = 50$ mins after switching off H_a. The sample was then warmed up to 15 K in zero-field condition, and $M(t)$ was measured again for $\Delta t_2 = 50$ mins where the corresponding graph displayed an exponential time decay. Finally, the initial temperature, i.e., 6 K was restored and $M(t)$ was observed to be independent of t when measured for $\Delta t_3 = 50$ mins. A discontinuity in the nature of the $M(t)$ vs. t curve during Δt_1 and Δt_3 measured at identical temperature conditions suggested a loss of the memory of the system. Hence, ZMCO does not retain its magnetic memory when subjected to a positive T-cycle.

4. Hierarchical versus Droplet Models for ZMCO:

To explain and understand the unidirectional memory response of ZMCO, we employed two SG models: Hierarchical model (HM) which was formulated by Dyson and Baker [36, 37] and Droplet model (DM) proposed by Fisher and Huse [13]. Since both models pose different theoretical descriptions of the SG phase, we had to determine the better choice for ZMCO. The HM features a multi-valleyed free energy landscape for $T < T_{SG}$ where metastable states ('valleys') separated by finite energy barriers are considered over pure states with infinite barriers. At any $T < T_{SG}$, these metastable states are assumed to continuously split into new states ('sub-valleys') upon decreasing the temperature, thus, resulting in a hierarchical energy landscape [36, 37]. On the contrary, the DM is characterized by only one pair of pure states where a characteristic correlation length comes into play for a group of spins. The correlation length gradually increases to infinity with time at any constant temperature, however, any temperature change (ΔT) destroys the existing correlation above a critical overlap length [13]. Hence, using Lefloch's approach and our experimental results from part (b) and (c), we tried to explain the asymmetric response of ZMCO to different T-cycles using both models [38].

During the negative T-cycle, DM can be used to explain the beginning of a new relaxation process at 6K (T-ΔT) by virtue of a rearrangement of spin correlations associated with ΔT change. However, it fails to explain the restoration of the initial relaxation behavior when system is warmed back to 15 K (T). According to DM, the system should have started a new aging process by virtue of ΔT change. Thus, DM fails to provide an explanation for the complete experimental picture during the negative T-cycle. On the other hand, according to HM, the system initially falls into a metastable state when quenched to T = 15K $< T_{SG}$, and eventually attains 'quasi'-equilibrium occupation probability for all states at 15K during Δt_1. When temperature is further lowered to 6K, HM predicts the splitting of the 'quasi'-equilibrium states into multiple sub-states. $\Delta T = 9$K is large enough to too large to ensure magnetic relaxation only within the sub-states. When temperature is raised back to 15 K, the sub-states in hierarchical energy landscape merge back to form the 'original' states, thereby, enabling history-dependent relaxation along the previous path. HM can be used to efficiently explain the positive T-cycle as well. The metastable states in which the system relaxes at $T = 6$K are lost due to merging of energy barriers at $T + \Delta T = 15$K. Now, during Δt_2, the system can relax within any 'quasi'-equilibrium state and follow an appropriate aging mechanism. When the initial temperature (6K) is restored, although the 'original' energy landscape is reestablished, the relative spin occupancies of each state had been altered when the system was allowed to age at 15K. So, intermediary heat treatment had destroyed the magnetic memory of the system and it now follows a time-independent path. Thus, HM successfully provides a clear understanding of why the negative T-cycle facilitates memory and rejuvenation effects in the SG phase of ZMCO while the positive T-cycle destroys the memory of the system. By our experimental investigation, we concluded that below T_{SG}, the free-energy landscape of ZMCO has a hierarchical nature which could be mapped onto a 'tree' structure with the end points of the 'branches' corresponding to manifold metastable states. Moreover, Dissado and Hill's correlated cluster model confirms that a hierarchical organization of metastable states possibly originates from 'cooperative' positional or orientational relaxation over spatially limited regions like clusters [39]. This further establishes a cluster SG phase in ZMCO below T_{SG}.

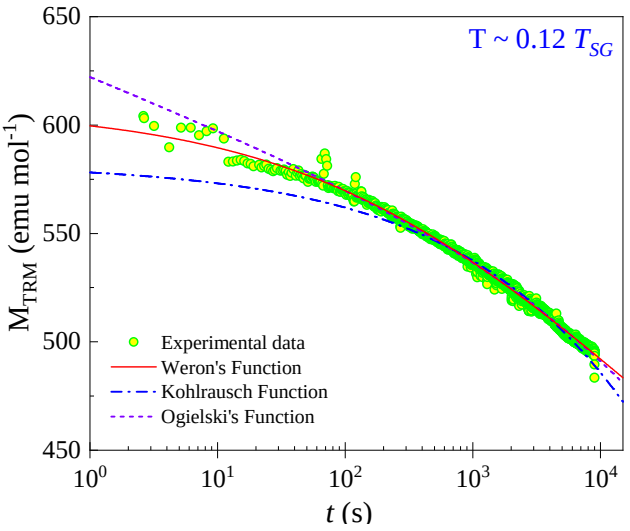

FIG. 3. Temporal dependency of the isothermal remanent magnetization of ZMCO measured at 4K (well within the SG phase) and its fit to different relaxation models are represented here. The experimental data (green-yellow circles) is best reproduced by Weron's function based on a purely stochastic theory which is represented by the red solid line. The purple 'short-dash' line is the fit to Ogielski's function, while the blue 'dash-dot' line represents the fit to Kohlrausch's relaxation functions.

E. Temperature dependence of the temporal decay of Isothermal Remanent Magnetization:

Thermal and temporal evolution of isothermal remanent magnetization (IRM) have been widely used to probe the field-quenched state realized in cluster SG systems and extract important information about the spin dynamics. In this section, we focus on the IRM behavior of ZMCO within the SG realm when subjected to thermal and temporal variations. For this study and subsequent analysis, the system was separately cooled down to five different temperatures corresponding to reduced temperature units $T_r = T_i/T_{SG} \sim 0.1$, 0.2, 0.3, 0.5, and 0.6, respectively. The cooling ensued under an applied field of magnitude +50 kOe. Upon stabilization of T_i, the magnetic field was turned off and the sample was allowed to age for a wait time (t_w) of 2.5h. For measurement at the next T_i, the sample was first heated back to its PM state and then the process was repeated. During t_w, the aging path followed non-trivial relaxation dynamics. The nature of decay could be better understood by investigating the fit to different relaxation mechanisms and interpreting the correct theoretical description of the underlying physical mechanism.

In this context, we tried to fit the IRM data for ZMCO with a semi-logarithmic time decay expression given by $M_{IRM}(t) = M_{IRM}(0) - Sln(t)$ S represents the magnetic viscosity of the system and $M_{IRM}(0)$ is the magnetization value immediately after the field is set to zero [23]. We observed an ill-fitting of the experimental data (not shown here), thus, leading us to reject the semi-logarithmic decay model for ZMCO. Similarly, the power law approach expressed as $M_{IRM}(t) = M_{IRM}(0)t^{-\gamma}$ ($M_{IRM}(0)$ = initial magnetization value instantly after the field is switched off, γ = decay parameter) did not work for ZMCO either and was also rejected [40].

Next, we applied three different models, namely, Kohlrausch's 'stretched-exponential' function, the Ogielski function and Weron's relaxation function, to the IRM data of ZMCO which yielded much better fits than the logarithmic and power law decay models. Fig. 3 contains the temporal variation of the relaxation isotherm of ZMCO obtained at T = 4K $< T_{SG}$ under FC condition and the corresponding least-square fits to the three above-mentioned relaxation functions. Kohlrausch's 'stretched-exponential' decay function has been frequently used to explain the anomalous relaxation in SG systems and is given by the equation: $\phi(t) = exp[-(t/\tau)^{\beta}]$ where $0 < \beta < 1$ [30, 41, 42]. Generally, when the exponent $\beta \to 0$, the asymptote represents a system with no magnetic relaxation, while $\beta = 1$ implies a monodispersive Debye-like relaxation involving only one time constant [30, 43]. In case of ZMCO, although the 'tail' of the relaxation isotherm at T = 4K (larger wait times) is well reproduced by the stretched-exponential, yet it failed to reproduce the beginning of the aging process as seen in Fig. 3. Upon adopting Ogielski's power law model, the relaxation dynamics could be better reproduced than Kohlrausch's function due to the addition of a power law pre-factor to the stretched exponential [44]. Ogielski proposed his model based on Monte Carlo simulations in a 3D ($\pm J$) Ising SG lattice, thus, yielding the mathematical form $\phi(t) = t^{-x}\, exp\,(\frac{-t}{\tau})^{\beta}$. The Ogielski function is subjected to two constraints: $0 < x \leq 0.5$ (around $\sim 4T_{SG}$) and $0 < \beta < 1$. The divergence of τ as $T \to T_{SG}^{+}$ would lead to a purely algebraic expression compatible with the scaling theory of critical phenomena [45]. Despite providing a fairly accurate mathematical representation of the IRM decay curve, Ogielski's function fails to determine the physical mechanism governing such non-exponential decay: whether caused by indepen-

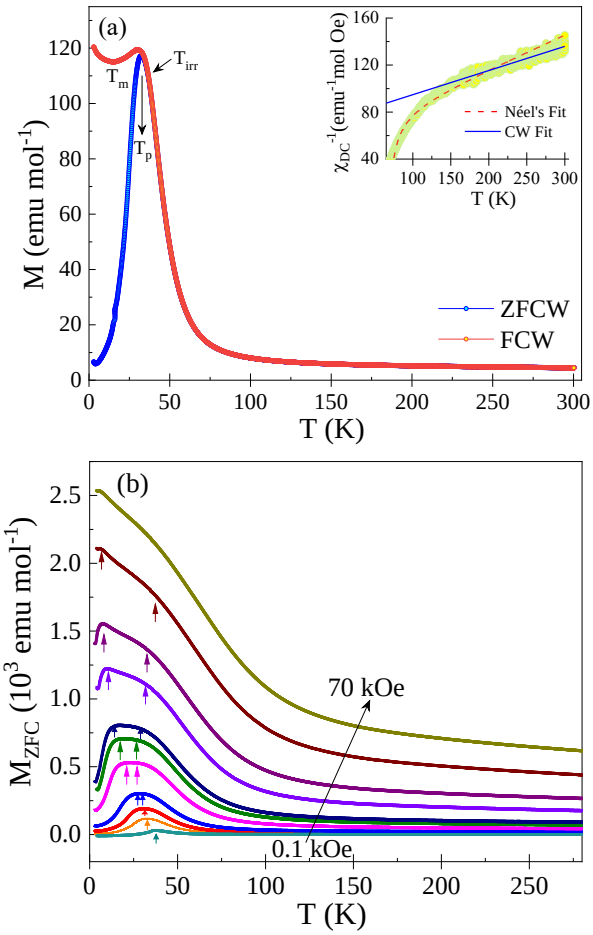

FIG. 4. (a) Temperature dependence of DC magnetization M(T) recorded under both ZFC (blue) and FC (red) warming conditions for an external field of 500 Oe. The peak temperature (T_p), FC-ZFC separation point (T_{irr}) and the minima in the FC curve (T_m) are marked in the figure. The inset displays the least-squares fits of the temperature dependence of inverse paramagnetic susceptibility to the CW and Néel's FiM models. (b) M_{ZFC} vs.T curves measured for various DC fields between 0.1-70 kOe which clearly established a two-peak behavior in ZMCO are shown in this figure.

dent (parallel) relaxation channels or by hierarchically constrained processes.

Finally, we tested Karina Weron's probabilistic model, originally proposed to describe the dielectric relaxation in systems whose behavior largely departed from the conventional Debye relaxation, similar to SG behavior [46]. This purely stochastic model is mainly based on a constantly evolving energy landscape due to hierarchical progression of relaxation processes. Weron's model involves two independent, non-negative random variables: waiting time (k_i) associated with the individual relaxation rate and dispersion rate (β_i) which reflects the waiting time for the local environment to attain equilibrium. The mathematical form of Weron's function that we used is given below [47, 48]:

$$\phi(t) = (1 + k(\frac{t}{\tau})^{\beta})^{-\frac{1}{k}};\ 0 < \beta \leq 1\ and\ k > 0 \qquad (1)$$

In eq. (1), τ represents the characteristic time constant for relaxation, β represents the fractal character and nature of relaxation in the SG system while k represents the hierarchical constraint on the dynamics associated with both inter and intra-cluster relaxation processes within the system. When $k \to 0$ for $T < T_{SG}$, Weron's function reverts back to a stretched exponential function, while for $k \to \infty$, eq.(6) asymptotically approached a logarithmic function. Our analysis yielded $0 < \beta \sim 0.4 < 1$, $k > 0$ for ZMCO below T_{SG}, comparable to other cluster SG systems such as $CoGa_2O_4$ ($\beta = 0.5$), $Fe_{17.8}Cr_{82.2}$ ($\beta = 0.3$ at T = 12 K) [48, 49]. The relaxation dynamics of other systems with a tendency for cluster formation have also been analyzed using Weron's model such as magnetically frustrated A-site spinels $CoAl_2O_4$ and $CoRh_2O_4$, metallic SG systems $Cu_{1-x}Mn_x$ and $Au_{0.86}Fe_{0.14}$, etc. [47, 50]. Moreover, based on Tsallis' report, we determined the non-extensive order parameter q for $T = 4$ K/$T_{SG} \ll 1$ in case of ZMCO by using the relation involving the interaction parameter $k = (q\text{-}1)/(2\text{–}q)$ [51]. According to previous reports on SG systems, q exhibits the following behavior: $q(T) \to 2$ (asymptotically) for $T/T_{SG} \ll 1$, $q(T_{SG}) = 5/3$, and $q(T) = 0$ for $T/T_{SG} \gg 1$ [48, 52]. In our case, we obtained $q(T) \sim 1.88$ when T = 4K ($\sim 0.12\ T_{SG}$). Hence, based on the detailed analysis of the IRM data, we were successful in demonstrating that Weron's generalized relaxation function based on the stochastic theory of dielectric relaxation could be experimentally reproduced by the IRM data of the cluster-glass system ZMCO and this relaxation model was better suitable in comparison to the Kohlrausch and Ogielski models throughout the entire observation time-scale [46]. Weron's model proves to be more reliable due to its global approach to glassy relaxation with a characteristic time constant, accounting for both intercluster and intracluster interactions, when subjected to a continuous structural reorganization of the energy landscape due to hierarchical progression of relaxations [46, 47]. Our memory effect studies also provide experimental confirmation of a hierarchical free-energy landscape within the cluster-glass regime.

F. Temperature dependence of DC-magnetometry:

Fig. 4(a) demonstrates the temperature-dependent DC magnetization measurements performed on the polycrystalline ZMCO sample following FC and ZFC warming protocols under an applied field of $H_{DC} = 500$ Oe. The M_{ZFC} curve underwent a huge bifurcation from its FC counterpart (M_{FC}(3K)-M_{ZFC}(3K) = $\Delta M \sim 114$ emu·mol^{-1}), starting around T_{irr} (~ 38.6 K) while exhibiting a prominent peak at a lower temperature centered around T_P (32.5 K). Strong thermomagnetic irreversibility is typical to SG or weakly FM systems and often attributed to two distinct magnetic phenomena: (i) spin-freezing due to frustrated interactions, and/or (ii) blocking of domain relaxation dynamics in anisotropic systems [23, 31]. The decrease of M_{ZFC} below T_P could be attributed to the random freezing of the clusters into different metastable states. On the other hand, the FC curve is expected to be flat below the SG transition, according to the mean-field theory. However, in our case, the magnetization initially decreases in the FCW mode starting from 3K, arrives at a shallow minimum marked as $T_m \sim 15$ K in Fig. 4(a) before increasing and finally peaking around T_p. Such a feature represents a non-trivial energy landscape of the FC state, also established in previous sections. Such characteristics of ZMCO under FC conditions contradicts the general perception of the FC state in SG systems as the equilibrium state, obtained via a simple 2nd order phase transition [53]. Fig. 4(b) shows $M_{ZFC}(T)$ measured at various H_{DC} values between 0.1 and 70 kOe under warming conditions. As H_{DC} increases, the peak in each $M_{ZFC}(T)$ curve broadens to form a plateau-like feature and hints at a two-peak behavior. Such peak broadening around T_p with increasing field in ZMCO is also well-documented in other cluster-glass systems [23, 31, 54, 55]. Next, the inverse of paramagnetic susceptibility (χ^{-1}(T)) at $H_{DC} = 100$ Oe was fitted to both Curie-Weiss (CW) law and Néel's ferrimagnetism (FiM) model as depicted in the inset of Fig. 4(a). Moreover, a gradual decrease in χ^{-1}_{DC} begins at higher temperatures in ZMCO which is indicative of the development of short-range magnetic correlations within the PM state. The best fit of our experimental data to the CW law, given by $\chi^{-1}_{DC} = (T + \theta_{CW})$/C yielded Curie constant C = 4.862 emu·K·mol^{-1}Oe^{-1} and a positive CW temperature $\theta_{CW} = 360.9$ K implying dominant AFM exchange interactions in ZMCO. In general, positive deviations from the Curie-Weiss line (solid blue line) correspond to fully compensated AFM interactions, whereas negative deviations as observed for ZMCO indicate FiM (uncompensated AFM) interactions [34, 54, 56–58]. Hence, Néel's FiM equation given below was further used to analyze ZMCO [57, 59]:

$$\frac{1}{\chi_{DC}} = \frac{T}{C} + \frac{1}{\chi_a} - \frac{\sigma_0}{T - \theta_0} \qquad (2)$$

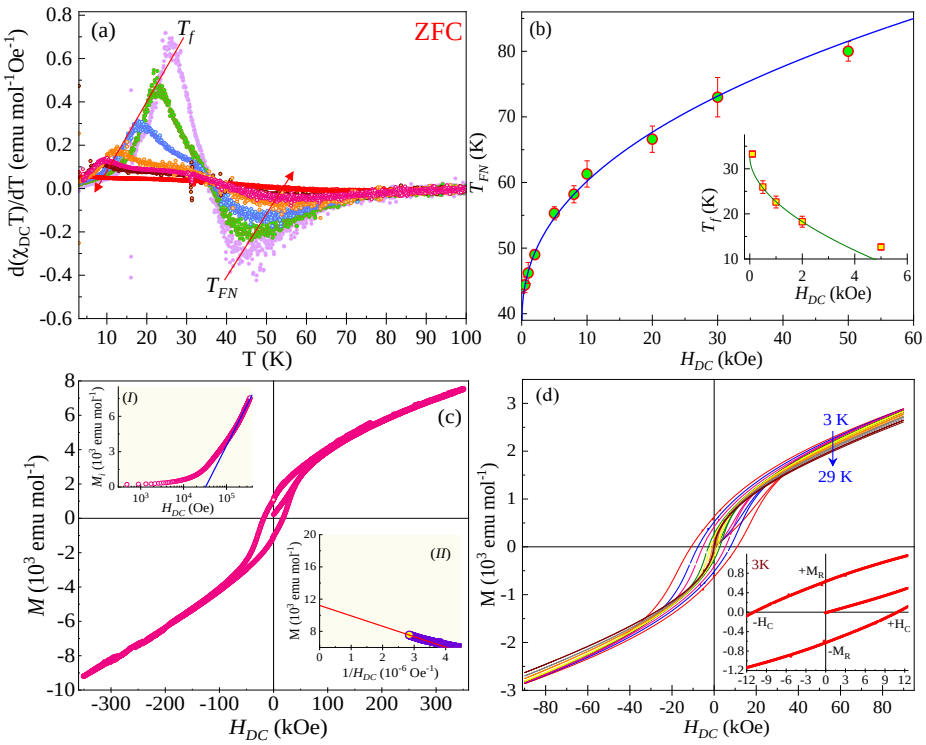

FIG. 5. (a) The 1st order derivative plots of DC susceptibility, d(χ_{DC}T)/dT versus T for ZMCO at different H_{DC} values are represented here and the arrows indicate the peak shift direction; (b) The main panel contains the H_{DC} dependence of the minima shown in part (b) while the inset shows the field variation of the peak temperature in (b). Both curves are provided with experimental error bars. The solid blue line shows the fit of the data to eq. (3) while the green line represents the best fit to eq. (4) at low fields. (c) M vs. H_{DC} isotherm recorded at T = 1.5 K using the high DC field facility at NHMFL is shown here. The five-cycle hysteresis loop is devoid of any signs of magnetic saturation even under very high field ($\sim$ 350 kOe) conditions. Inset (I) shows the initial magnetization curve in the first quadrant with a power-law fit of the high field data. Inset (II) represents the plot of M vs $1/H_{DC}$ at T = 1.5 K for $H_{DC} > 220$ kOe which was extrapolated to the limit, $1/H_{DC} \rightarrow 0$ in an attempt to obtain the saturation magnetization value for ZMCO. (d) Isothermal hysteresis loops obtained separately at different temperatures (3K $\leq$ T $<$ 30 K) during a field change cycle of 0 Oe $\rightarrow$ 90 kOe $\rightarrow$ -90 kOe $\rightarrow$ 0 Oe $\rightarrow$ 90 kOe are shown here. The inset illustrates appreciable coercivity at low temperatures.

This analysis provided a better fit (dashed red line) in comparison to the CW model and yielded total Curie constant C $\sim$ 3.497 emu·K·mol^{-1}Oe^{-1}, $|\theta_0| \sim$ 63.4 K, $\sigma_0 \sim$ 497.3 Oe·K·emu^{-1}, and χ_a = 0.0162 emu·mol^{-1}Oe^{-1}. Using these values, we first extracted the effective magnetic moment per f.u., μ_{eff}/f.u. $= (3k_BC/N_A)^{1/2}\mu_B$ where N_A = Avogadro's number/mole, k_B = Boltzmann's constant and μ_B = Bohr magneton. Here, only magnetic Mn^{3+} ions ([Ar]3d^4) are expected to contribute to μ_{eff} since diamagnetic Zn^{2+}([Ar]3d^{10}4s^2) has no unpaired electrons and octahedral Co^{3+} ([Ar]3d^6) usually attains a low-spin (LS) state ($\mu_{Co-LS} = 0$) [7]. Our experimental μ_{eff} value (see Table I) is slightly higher than the theoretical value for one high-spin Mn^{3+}(= 4.9 μ_B) ion per f.u. [60]. This enhanced μ_{eff} value could be attributed to octahedral Co^{3+}. Previously, Cossee discovered weak PM contributions from octahedral Co^{3+} in $ZnCo_2O_4$ to μ_{eff} due to a small energy gap between its diamagnetic and PM states in an octahedral environment set up by oxygen ligands [7]. The possibility of a mixed spin-state of Co^{3+} was discarded since the FWHM ($\sim$ 1.87 eV) of the Co-2$p_{3/2}$ XPS peak (see Fig. S1(c)) matched with that of pure LS Co^{3+} ions possessing spin-paired t_{2g} and empty e_g orbitals [18, 61]. Our value of g_{eff} is 8% higher than the spin only value $g_0 = 2$. Both parameters are related by $g_{eff} = g_0\ (1 \pm K/\Delta)$ where K is associated with spin-orbit coupling (SOC) and Δ corresponds to CF splitting [62]. TM ions in octahedral complexes generally experience quenching of their orbital angular moment due to strong CF effects implying negligible SOC contribution (K = 0; $g_{eff} = g_0$). However, in case of ZMCO, there seems to be some orbital mo-

TABLE I. This table contains the list of magnetic parameters obtained from fits to the CW and Néel's FiM models.

Magnetic Parameters	CW Law	Néel's FiM model
C	4.862 emu·K·mol^{-1}Oe^{-1}	3.495 emu·K·mol^{-1}Oe^{-1}
$\mu_{eff}/f.u.$	$6.24\mu_B$	$5.28\mu_B$
g_{eff}	2.55	2.16
μ_z	$5.10\mu_B$	$4.32\mu_B$
M_s	28474.9 emu·mol^{-1}	24119.9 emu·mol^{-1}

ment contribution due to SOC. Table I lists significant magnetic parameters computed from the fits to CW and FiM models. The asymptotic Curie temperature associated with the magnetic exchange coupling strength of the system was also evaluated $T_{ACW} = \mathrm{C}/\chi_a \sim 215.9$ K.

The temperature derivative of DC susceptibility, i.e., d(χ_{DC} T))/dT vs T allowed for better visualization and determination of the critical transitions in ZMCO (see Fig. 5(a)). For each H_{DC}, two pronounced anomalies were observed, a lower temperature peak (T_f) assigned to a spin-freezing phenomenon and a minimum at a higher temperature (T_{FN}) ascribed to FiM ordering with short-range magnetic correlations. The nature of shift in both anomalies with increasing H_{DC} was investigated to justify the presence of two different magnetic phenomena. The minima were field-sensitive and their H_{DC}-variation was fitted to the following equation as shown in the main panel of Fig. 5(b) [57]:

$$T_{FN} = T_{FN}(0) + A_1 H^p \tag{3}$$

With increase in H_{DC}, the curve exhibited a non-monotonous shift to higher temperatures, confirming FiM-type behavior in ZMCO above the SG realm [57, 59]. However, specific heat analysis discussed in a later section indicates a lack of any long-range magnetic order in ZMCO down to the lowest temperatures, i.e., the FiM behavior must be short-ranged (FiM(SR) phase). Coexistence of FiM and SG phases or the presence of FiM clusters with short-range magnetic correlations in TM spinels have been previously reported [34, 54, 58, 63]. The fit to eq. (3) yielded $T_{FN}(0) = 37.9$ K, $p = 0.41$ and $A_1 = 8.5$ K (Oe)$^{-0.41}$. In case of an ideal ferromagnet, the expected value for p is 0.20 according to Landau's theory as magnetization directly couples with H_{DC} [64]. In existing reports, $p = 0.15$ (FM) for $La_{0.7}Sr_{0.3}MnO_3$ thin films while bulk sample of $Ni_4Nb_2O_9$ generated $p = 0.35$ (FiM) [57, 64]. Since ZMCO is argued to have a FiM(SR) phase, the shift of T_{FN} with respect to H_{DC} is much smaller than that for a ferromagnet or long-range ordered ferrimagnet, thus, generating a much larger p value.

Conversely, T_f shifted towards lower temperatures as H_{DC} increased (see inset of Fig. 5(b)), most likely due to field-induced suppression of energy barriers. Such behavior is typically observed in case of frustrated cluster SG or anisotropic FiM systems [54]. In our case, we assign this peak to a cluster SG phase transition and the shift could be well fitted by the following power law expression at low fields [23]:

$$H_{DC}(T) = A^{-\phi}(1 - T_f(H_{DC})/T_{SG})^{\phi} \tag{4}$$

T_{SG} is the SG transition temperature where the M_{ZFC} curve is expected to peak in the absence of an external magnetic field, coefficient A depends on factors such as anisotropy strength, variance of random exchange and number of spin components, while ϕ is known as the crossover exponent which also depends on the anisotropy strength with respect to the magnetic field. $\phi = 0.67$ indicates strong anisotropy corresponding to a mean-field AT line for Ising spins while $\phi = 2$ represents the Gabay-Toulouse (GT) line predicted for Heisenberg spin systems with weak anisotropy [65, 66]. Our fit to eq. (4) yielded $T_{SG} = 32.65$ K, $\phi \sim 0.53$ and $A = 0.304$ Oe$^{-0.53}$. Hence, ZMCO belongs to a different universality class in the strong anisotropy regime, following an AT line with non-mean-field instability in the investigated H-T plane. This anisotropy is established by a frustrated network of Co^{3+} and Mn^{3+} ions which promotes large disorder in the system. Several SG systems have been reported to exhibit non-mean field AT behavior, such as $ZnTiCoO_4$ ($\phi \sim 0.50$), $Cr_{0.5}Fe_{0.5}Ga$ ($\phi \sim 0.53$), MnCu ($\phi \sim 0.4$) [23, 30, 67]. We also calculated the frustration ratio for ZMCO, $f_r = |T_{ACW}|/T_{FN}(0) \sim 6 > 1$ which signifies appreciable magnetic frustration in the system.

G. Field dependence of DC-magnetometry:

The five-cycle M vs. H_{DC} loop was measured at 1.5 K by varying the magnetic field in the range -350 kOe $\leq H_{DC} \leq$ 350 kOe (see Fig. 5(c)). Despite very high fields, the M-H_{DC} loop exhibited no saturation tendency, a giant coercive field $H_c \sim 17.8$ kOe and non-zero magnetic retentivity. The 'S' shaped hysteresis curve is characteristic of a SG phase and possibly arises from unequal moments, uncompensated/canted spin configuration within the magnetic clusters [23, 31, 68]. Further, the existence of hysteresis in ZMCO eliminated superparamagnetism as a candidate for its magnetic ground state, also verified by NAL analysis [45]. The 'virgin'

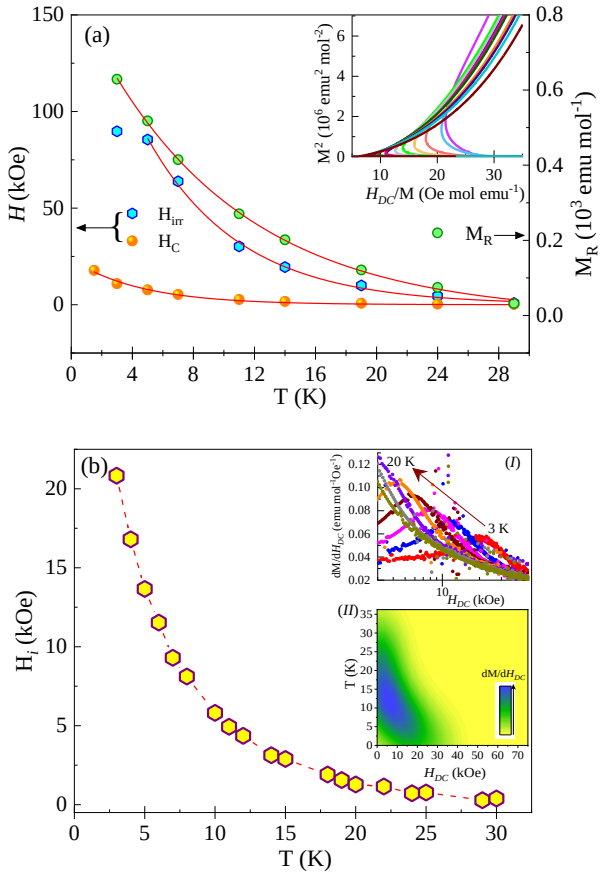

FIG. 6. (a) Temperature variation of magnetic hysteresis loop parameters, namely, coercive field H_c(T), magnetic remanence M_R(T) and irreversibility field H_{irr}(T) obtained under isothermal conditions ranging between 3-30 K. M_R (right-hand scale) and H_C and H_{irr} (left-hand scale) had decent fits to eqs. (10), represented by red solid lines. The inset contains the conventional Arrott plots for the sample; (b) Thermal evolution of the peak position in the computed dM/dH_{DC} vs H_{DC} plots (shown in inset (I)) between 3 K and 20 K is shown here. Inset (II) shows a contour representation of the field-induced transition in ZMCO.

magnetization M_i vs. H_{DC} curve at 1.5 K is represented as a semilogarithmic plot in the inset (I) of Fig. 5(c). Initially, at lower fields, M_i increases slowly followed by a 'steep' power law increase (solid blue line shows a linear fit) at higher fields, which is characteristic of SG-like spin freezing in the system [69, 70]. Although there is no hint of saturation, we linearly extrapolated the value of magnetization in the M_i vs $1/H_{DC}$ plot (see inset (II) of Fig. 5(c)). This yielded $M_{exp} = 11217 \pm 31$ emu·mol^{-1} in the limit $1/H_{DC} \rightarrow 0$ which is significantly smaller than the theoretical value listed in Table I which confirms a frustrated magnetic ground state. Isothermal M-H_{DC} sweeps for eight temperatures between 3-30 K are shown in the inset of Fig. 5(d) which enabled us to study the temperature variation of H_C, remanence M_R and irreversibility field H_{irr} where the hysteresis loop closes. The T-variations of all three above parameters are presented in the main panel of Fig. 6(a) where H_C, H_{irr} and M_R varied exponentially:

$$H_x(T) = H_x(0)\, exp\,(-\alpha_H(x)T); x = C, irr$$

$$M_R(T) = M_R(0)\, exp\,(-\alpha_M T) \quad (5)$$

The fits generated important parameters such as $H_C(0)$ = 23.54 ± 1.3 kOe/f.u. and $M_R(0)$ = 865 ± 9 emu·mol^{-1}/f.u. along with the fitting constants $\alpha_H(C)$ = 0.22 ± 0.02 and α_M = 0.104 ± 0.001. Such thermal response of H_C and M_R is distinctive of 'glassy' characteristics [71]. The fit for H_{irr}(T) variation was not reliable at lower temperatures. Also, H_C, M_R and H_{irr} values rapidly approached zero as $T \rightarrow T_{SG}$. The conventional Arrott plots for the sample (inset of Fig. 6(a)) were briefly analyzed to unearth the field-induced magnetism in ZMCO. A negative intercept of the conventional Arrott plots (M^2 versus H_{DC}/M) for ZMCO at all temperatures suggested the absence of spontaneous magnetization. Moreover, the distorted S-shape of the plots, negative curvature, non-linear M^2 curves with positive slopes at low fields reaffirmed the presence of short-range magnetic correlations and complex field-induced magnetism in ZMCO. In continuation, isothermal M vs. H_{DC} plots in the first quadrant were used to compute dM/dH_{DC}. A broad transition around H_i was observed whose temperature dependence is represented in the main panel of Fig. 6(b). Such a transition is often associated with H_{DC}-induced domain/cluster reorientation [72, 73]. With increasing temperature, the peak position rapidly decreases to lower H_i values (inset(I) of Fig. 6(b)) while the peak amplitude increases which is illustrated by a 2D contour map (inset(II) of Fig. 6(b)).

H. Temperature and field dependency of the 'Glassy' clusters:

This section deals with the external field and thermal effects on the clusters in the SG phase of ZMCO by analysing the virgin M-H_{DC} isotherms. A systematic mathematical fit of the 1^{st}-quadrant M vs. H_{DC} data at different temperatures was obtained using the modified Langevin equation [74]:

$$M = N\mu L(\alpha) + \chi_f H_{DC} \quad (6)$$

In the above expression, Langevin function L(α) = $coth(\alpha) - \frac{1}{\alpha}$ where $\alpha = \mu H_{DC}/k_B T$, and χ_f is the field-dependent Curie-type susceptibility associated with intrinsic magnetization of the system. On the other hand, N represents the number of magnetic entities per unit mass of sample while μ is the magnetic moment per cluster in μ_B units. At the lower fields, the contribution from μ dominates whereas at higher fields, the χ_f term dominates. A slight deviation of the fitted curve from the

experimental data at low temperatures is likely associated with the cluster-freezing phenomena under external field effects referred to earlier, which is not accounted for in eq (6). The main panel of Fig. 7 displays Langevin fits to only a few isotherms spanning the temperature range 1.5-30 K where each plot is offset along the y-axis in equidistant measures to prevent their overlap. This analysis reveals that μ increases while N decreases as the temperature increases (see inset of Fig. 7). With decreasing temperature, the SG phase strengthens leading to smaller magnetic clusters and in turn, decreased magnetic moment per entity [74]. The average diameter d of the clusters at low temperatures was 1.6±0.5 nm, as roughly estimated using the sample density = 5.86(3) g/cm^3 from RSR and the temperature-dependent fitted parameters N and μ. Nevertheless, a detailed field-dependent small-angle neutron scattering (SANS) is warranted to accurately determine the size of such tiny localized spin clusters.

I. Thermal variation of specific-heat:

The main objective of analyzing the temperature dependence of molar specific-heat capacity ($C_p(T)$) of ZMCO recorded at H_{DC} = 0 and H_{DC} = 90 kOe was to establish the nature of magnetic order in the system and the results are presented in Fig. 8. The absence of an asymmetric 'λ'-like peak and instead, the presence of weak anomalies highlight the following for ZMCO: (i) no long-range magnetic order and (ii) short-ranged magnetic correlations. The phonon contribution C_{ph} to $C_p(T)$ was extracted by employing the combined Debye-Einstein (DE) model given below [75]:

$$C_{ph} = C_{Debye} + C_{Einstein}$$

$$= 3Ra_D x_D^{-3} \int_0^{x_D} \frac{x^4 e^x}{(e^x-1)^2}\,dx + R\sum_i b_{E_i} \frac{x_{Ei}{}^2 e^{x_{E_i}}}{(e^{x_{E_i}}-1)^2} \quad (7)$$

For eq. (7), R is the universal gas constant, x_{D,E_i}=$\frac{\theta_{D,E_i}}{T}$ is the reducible representation of inverse temperatures where θ_D is the Debye temperature and θ_{E_i} is the Einstein temperature while i is the index variable for an optical mode of vibration. C_{Debye} is related to acoustic phonon modes whereas $C_{Einstein}$ is a sum of the contributions from optical modes to the C_{ph} spectrum. The DE model states that the ratio of the relative weights of acoustic modes and sum of all optical modes is equal to 1:m-1. For spinels, m which denotes the number of atoms per f.u. is 7. For ZMCO, we considered the distribution of 21 lattice degrees of freedom (DOF) over acoustic and optical modes in a manner such that the 18 optic modes are distributed among 2 Einstein oscillators (b_{E1} and b_{E2}) while the remaining are all acoustic modes (a_D). Following this distribution, a satisfactory fit was obtained in the high temperature regime where phonon contributions dominate which yielded θ_D = 283.4 ± 2.8 K, θ_{E_1} =

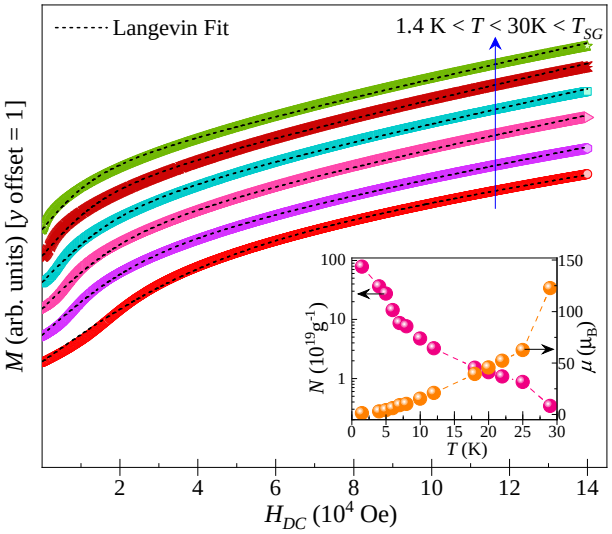

FIG. 7. Langevin fits to few isothermal $M-H_{DC}$ curves in the range 1.5 - 30 K are shown here, with each plot equidistantly offset along the y direction for better visualization. The inset shows the temperature variation of the effective moment per cluster (μ) in μ_B units and the number of clusters per unit mass of sample (N) in g^{-1} units extracted from the Langevin fitting.

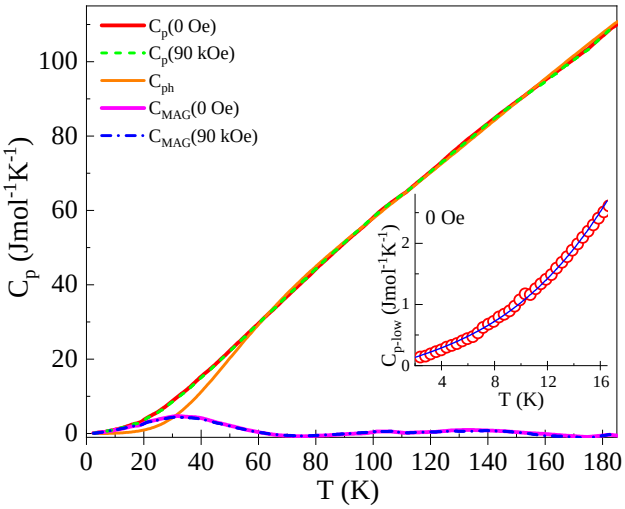

FIG. 8. Temperature dependence of the molar specific heat capacity C_p(T) of ZMCO recorded under both zero-field (H = 0 Oe) and high field (H_{DC} = 90 kOe) conditions. The individual contributions of magnetic behavior (C_{MAG}) and lattice vibrations (C_{ph}) obtained from the fit to the Debye-Einstein Model (eq. (12)) are also shown in the main panel of the figure. Please refer to the legend provided for accurate identification of each curve. The inset provides a decent fit of C_{p-low}(T) data to eq. (13) under zero field conditions in the low temperature region where the SG phase prevails.

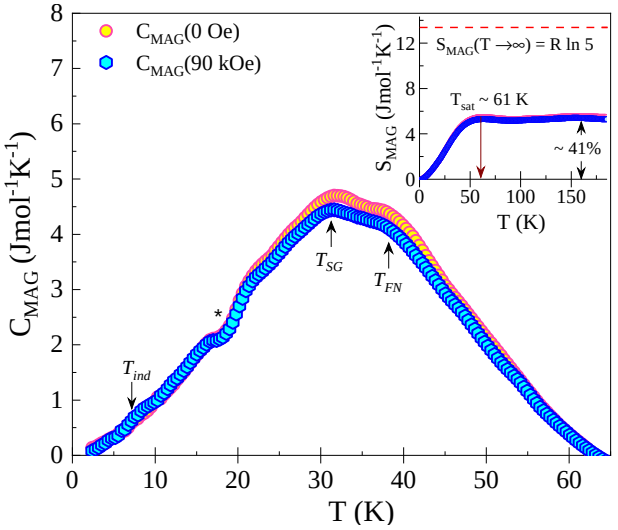

FIG. 9. Temperature dependence of C_{MAG} for ZMCO under both field conditions, below 60K where the magnetic contribution is most significant. On the other hand, the inset contains the temperature variation of magnetic entropy for the system, S_{MAG}, which is computed by the numerical integration of the C_{MAG}/T data and saturates around $T_{sat} \sim 61$ K. S_{MAG} accounts for only 41% of the expected theoretical value. The red dashed line in the inset marks the theoretical spin-only S_{MAG} value which would prevail if ZMCO exhibited a conventional long-range magnetic order.

788.2 ± 2.5 K and $\theta_{E_2} = 231.3 \pm 1.7$ K. Below 60 K, magnetic contributions to $C_p(T)$, referred to as C_{MAG} gain prominence resulting in a deviation from the DE model and was obtained by subtracting C_{ph} from $C_p(T)$. For more insight into ZMCO's magnetic behavior, at quite low temperatures and zero field conditions, the $C_p(T)$ plot within the SG state, termed as $C_{p-low}(T)$, could be well reproduced by the following equation [28, 30]:

$$C_{p-low}(T) = \gamma' T + \beta' T^3 + \delta' T^{3/2} \quad (8)$$

The inset of Fig. 8 displays $C_{p-low}(T)$ along with the fit to eq.(8) obtained under zero field condition. The Sommerfeld coefficient $\gamma' \sim 64$ mJ/mol K^2 for ZMCO is similar to that reported for other insulating SG systems like $PrRhSn_3$, $Cr_{0.5}Fe_{0.5}Ga$, etc. [28, 30]. Such high value is consistent with cluster-glass behavior and the linear T-dependent term results from constant low-energy magnetic fluctuations due to frustration and manifold degenerate ground states. The 2^{nd} term in eq.(8) with $\beta' = 3.3\times10^{-4}$ J/mol K^4 represents the Debye-T^3 law while the 3^{rd} term with a $T^{3/2}$ dependency is due to spin-wave-like excitations at low temperatures, observed in certain SG systems [28, 30, 76, 77]. An enlarged view of C_{MAG} (see Fig. 9) obtained at both field conditions reveals a broad hump with anomalies close to the transition temperatures also observed from our magnetometry studies. A small hump around T_{ind} is only observed in the C_{MAG} curve recorded at 90 kOe. The position of T_{ind} which is in line with the observations in Section G for 90 kOe, confirms the presence of a field-induced transition in the system associated with the spin-cluster dynamics of ZMCO. An additional kink across ~ 18 K, marked as * was also observed which could not be identified through magnetometry techniques. Although its true origin remains uncertain, it could possibly be attributed to cluster/domain effects within the SG phase of ZMCO. However, the kink may also appear due to limitations of our analysis since C_{MAG} is not measured directly but obtained by subtracting the phonon contribution from the total $C_p(T)$. Another typical low temperature SG signature is a power law temperature dependence of C_{MAG}, ideally with an exponent ~ 1.5. For ZMCO, C_{MAG} was observed to follow the relation $C_{MAG} = \phi T^{1.55}$ with $\phi = 27$ mJ mol^{-1}K$^{-2.55}$ at temperatures well below T_{SG} as shown in Fig. S3 in SI [18].

Subsequently, the magnetic entropy, S_{MAG} of ZMCO was extracted from the equation: $S_{MAG} = \int_{T_{min}}^{T} \frac{C_{MAG}}{T}\, dT$ (here, $T_{min} = 2.4$ K) and its temperature dependence under $H_{DC} = 0$ and 90 kOe are presented in the inset of Fig. 9. The magnetic entropy saturates around 61 K at a magnitude of 5.5 (5.3) Jmol^{-1}K^{-1} for $H_{DC} = 0$ Oe (90 kOe). The slightly lower magnitude of S_{MAG} for $H_{DC} = 90$ kOe than that for $H_{DC} = 0$ Oe is expected due to the imposed magnetic spin alignment in PM state caused by an external field. However, in comparison to the theoretically estimated value of $S_{MAG} \sim 13.4$ Jmol^{-1}K^{-1}, obtained using $S_{MAG} = R\ln(2S + 1)$ for S = 2, the experimental value was highly suppressed and accounted for only 41% of the theoretical value expected for only spin DOF. Such observation in ZMCO corroborates the presence of frustration and multiple degenerate low-energy states at low temperatures which holds true for a SG ground state. In conclusion, S_{MAG} of ZMCO was significantly small for the development of long-range magnetic order [23, 28, 48].

To represent all our experimental findings in one figure, we constructed the phase diagram of ZMCO and plotted it in the temperature-field plane as shown in Fig. 10. ZMCO evolves through a series of magnetic transitions owing to the complexity of its spin dynamics, but fails to attain any long-range magnetic order under the effect of frustration and disorder. On cooling the system from 300 K where the system behaves like a paramagnet, short-range magnetic correlations emerge below 180 K, represented by the dotted line ***I*** indicating the intermediate state, PM+SRC. On further cooling, the system undergoes a transition from the PM+SRC dual-phase to a FiM(SR) phase and the transition line ***II*** distinctly demarcates the two phases. When the temperature is further lowered, the system undergoes yet another phase transition to a cluster SG phase, characterized by a 'hierarchical' free energy landscape and separated from the FiM(SR) phase by the transition line ***III***. All transitions and their short-range nature were well corroborated by *ac*-susceptibility and heat capacity studies on ZMCO. Details of the origin of the separate phases have

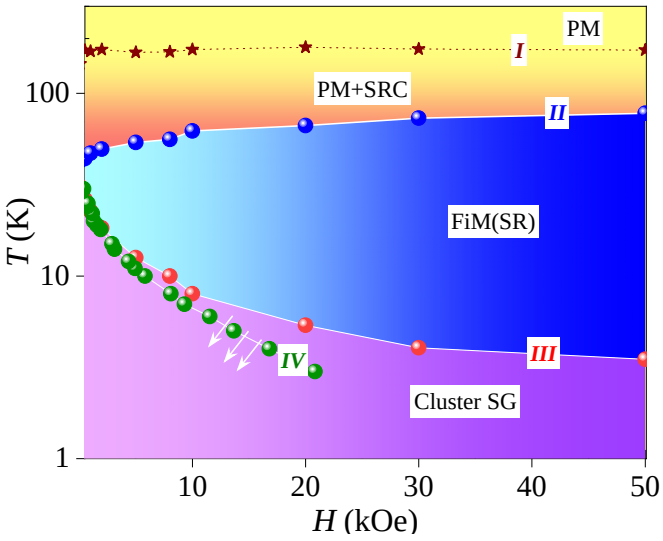

FIG. 10. The phase diagram of ZMCO is mapped out on the $T-H$ plane where the major phase transition lines are highlighted and numbered (***I***, ***II***, ***III***, and ***IV***). The experimental data are connected by straight lines which act as visual guides.

already been elaborated upon in earlier sections. It is interesting to note that although the separation between the FiM(SR) and cluster SG phases decreases on reducing the strength of the external DC magnetic field, yet, the two phases never merge. Further, a field-induced transition line ***IV*** lies within the SG realm. For $H \leq$ 2 kOe, line ***IV*** coincides with line ***III***. Beyond $H >$ 2 kOe, they start to slightly bifurcate with a progressive increase in the separation between them as external DC field increases. As mentioned earlier, this transition is likely due to domain/cluster reorientation effects assisted by strong DC fields. Stronger the magnitude of external magnetic field, greater is the separation between the transition lines. The magnetic phase diagram of another trication spinel $ZnTiCoO_4$ yields three distinct phases: cluster SG, AFM with short-range magnetic order and the high temperature PM phase, whereas the cluster-glass system Co_2RuO_4 undergoes multiple transitions from PM to AFM to cluster SG [23, 31]. Some cluster-glass systems such as trication $LiFeSnO_4$, $Cr_{0.5}Fe_{0.5}Ga$ undergo only one magnetic transition from PM to SG, demarcated by the AT line with different values of the ϕ in eq. 4 (mean-field or non-mean-field) [30, 78].

IV. SUMMARY AND CONCLUSIONS

Polycrystalline (Zn)[MnCo]O_4, chemically synthesized in the single phase using solid-state technique, attains a Fd-3m crystal symmetry and exhibits a cluster SG ground state. The substitution of 50% octahedral Mn^{3+} by Co^{3+} cations in $ZnMn_2O_4$ facilitated two intriguing features: (i) elimination of Jahn-Teller (JT) lattice distortion due to JT-active Mn^{3+}, and (ii) destruction of long-range AFM order in the system. The incorporation of Co^{3+} cations at half of the Mn^{3+} sites in the B sublattice rendered the JT effect of the remaining Mn^{3+} insufficient in relieving frustration in ZMCO by structural distortion. A complicated magnetic behavior was observed for the system. The trivalent Co ions at B-sites prefer LS configuration when in octahedral coordination. Such effects resulted in dilution of the magnetic interactions where both A-A and A-B magnetic exchanges were missing and only 50% of the B-B exchanges were expected to contribute to the magnetic nature of the system. DC and ac magnetometry data analysis unveiled short-range magnetic order leading to a FiM(SR) phase (T_{FN} = 37.9 K) followed by a cluster SG phase (T_{SG} = 32.6 K). A negative deviation from the ideal CW line also confirmed FiM interactions (uncompensated AFM behavior) in the system. The dominant NN exchange interactions in ZMCO were AFM in nature. The cluster glass phase was thoroughly investigated by monitoring thermal and temporal evolution of the system under various measurement protocols including IRM measurements. The 'non-exponential' relaxation spin dynamics in ZMCO within the SG phase was best reproduced by Weron's function in comparison to other SG relaxation models. An asymmetric response of ZMCO to positive and negative T-cycles supported a 'hierarchical' free-energy landscape for ZMCO. In other words, the system ages non-ergodically and remains 'trapped' in a main energy 'valley' upon lowering the temperature, thus, retaining its past memory. The robustness and non-volatility of the unidirectional memory of the system, exhibited only during the negative T cycle, could be exploited for technological advancement in multi-level storage media and spintronics. A moderately large coercivity without any exchange bias could possibly result from isolation of the magnetic clusters due to weak inter-cluster interaction which was quantified by Ω = 0.013 for ZMCO. The presence of weak anomalies instead of a 'λ'-shaped anomaly in the specific heat data also ruled out long-range magnetic order in ZMCO. S_{MAG} could account for only 41% of the theoretical spin-only value expected for a complete ordering of all S = 2 (Mn^{3+} in HS state) spins. Hence, an appreciable frustration in the system was proved. The current experimental investigation not only provides deep insights into a real correlated system with properties modulated by combined effects of disorder, random anisotropy and frustration, but also opens pathways for future exploration of subsequent doping effects on ZMCO by employing neutron diffraction and SANS measurements.

ACKNOWLEDGMENTS

MRC acknowledges the Ministry of Education, Government of India, for providing financial support through the Prime Minister's Research Fellowship (PMRF ID:

1901274) May 2021 scheme. ST acknowledges the DST SERB Core Research Grant File No. CRG/2022/006155 for the partial support of this work. MRC and ST acknowledge the FIST program of the DST, India, for partial support of this work (Grant Nos. SR/FST/PSII-020/2009 and SR/FST/PSII-037/2016). TS acknowledges financial support from the Swedish Research Council (VR Grant No. 2021-03675). Authors express their sincere thanks to Dr. Rajeev Rawat of UGC-DAE CSR, Indore. This work was partially carried out using the facilities of UGC-DAE CSR. The authors acknowledge the financial support from UGC-DAE CSR through a Collaborative Research Scheme (CRS) project number CRS/2021-22/09/849. A portion of this work was performed at the National High Magnetic Field Laboratory, which is supported by National Science Foundation Cooperative Agreement No. DMR-2128556 and the State of Florida. MRC acknowledges the NIMS Internship Program. MRC and ST acknowledge the Central Instrument Facility and Department of Physics of IIT Guwahati for their support. MRC expresses her sincere thanks to Dr. Sayandeep Ghosh and Dr. Deep Chandra Joshi for helpful discussions.

[1] V. Tsurkan, H.-A. K. Von Nidda, J. Deisenhofer, P. Lunkenheimer, and A. Loidl, Physics Reports **926**, 1 (2021).
[2] S.-H. Lee, H. Takagi, D. Louca, M. Matsuda, S. Ji, H. Ueda, Y. Ueda, T. Katsufuji, J.-H. Chung, S. Park, *et al.*, Journal of the Physical Society of Japan **79**, 011004 (2010).
[3] J. A. Mydosh, *Spin glasses: an experimental introduction* (CRC Press, 1993).
[4] P. Charbonneau, E. Marinari, G. Parisi, F. Ricci-tersenghi, G. Sicuro, F. Zamponi, and M. Mezard, *Spin Glass Theory and Far Beyond: Replica Symmetry Breaking after 40 Years* (World Scientific, 2023).
[5] P. Patra, I. Naik, H. Bhatt, and S. Kaushik, Physica B: Condensed Matter **572**, 199 (2019).
[6] S. Åsbrink, A. Waśkowska, L. Gerward, J. S. Olsen, and E. Talik, Physical Review B **60**, 12651 (1999).
[7] P. Cossee, Recueil des Travaux Chimiques des Pays-Bas **75**, 1089 (1956).
[8] Y. Ikedo, J. Sugiyama, H. Nozaki, H. Itahara, J. Brewer, E. Ansaldo, G. Morris, D. Andreica, and A. Amato, Physical Review B **75**, 054424 (2007).
[9] P. Pramanik, D. C. Joshi, M. Reehuis, A. Hoser, J. Hoffmann, R. Manna, T. Sarkar, and S. Thota, Journal of Physics: Condensed Matter **32**, 245801 (2020).
[10] A. Baby, B. Senthilkumar, and P. Barpanda, ACS Applied Energy Materials **2**, 3211 (2019).
[11] C. Xu, B. Li, H. Du, and F. Kang, Angewandte Chemie International Edition **51**, 933 (2012).
[12] S. Sun, Y. Sun, Y. Zhou, J. Shen, D. Mandler, R. Neumann, and Z. J. Xu, Chemistry of Materials **31**, 8106 (2019).
[13] D. S. Fisher and D. A. Huse, Physical Review B **38**, 373 (1988).
[14] M. Castellana and C. Barbieri, Physical Review B **91**, 024202 (2015).
[15] R. G. Palmer, D. L. Stein, E. Abrahams, and P. W. Anderson, Physical Review Letters **53**, 958 (1984).
[16] J. S. Hwang, K. J. Lin, and C. Tien, Review of scientific instruments **68**, 94 (1997).
[17] I. U. of Crystallography, *Symmetry groups, edited by NFM Henry and K. Lonsdale*, Vol. 1 (Kynock Press, 1952).
[18] See Supplemental Information File.
[19] W. H. Bragg, The London, Edinburgh, and Dublin Philosophical Magazine and Journal of Science **30**, 305 (1915).
[20] N. Grimes, Physics in Technology **6**, 22 (1975).
[21] J.-C. Dupin, D. Gonbeau, P. Vinatier, and A. Levasseur, Physical Chemistry Chemical Physics **2**, 1319 (2000).
[22] R. K. Dokala, S. Das, D. C. Joshi, S. Ghosh, Z. Yan, Y. Qi, S. Das, and S. Thota, Journal of Applied Physics **127** (2020).
[23] M. R. Chowdhury, M. S. Seehra, P. Pramanik, S. Ghosh, T. Sarkar, B. Weise, and S. Thota, Journal of Physics: Condensed Matter **34**, 275803 (2022).
[24] P. Pramanik, D. Joshi, N. Tiwari, T. Sarkar, S. Pittala, O. Salman, M.-M. Manga, and S. Thota, Journal of Applied Physics **125** (2019).
[25] L. Twigge, J. Conradie, and E. Erasmus, Journal of Chemical Research **47**, 17475198231184788 (2023).
[26] A. Rosencwaig, G. Wertheim, and H. Guggenheim, Physical Review Letters **27**, 479 (1971).
[27] P. Pramanik, S. Thota, S. Singh, D. C. Joshi, B. Weise, A. Waske, and M. Seehra, Journal of Physics: Condensed Matter **29**, 425803 (2017).
[28] V. Anand, D. Adroja, and A. Hillier, Physical Review B **85**, 014418 (2012).
[29] S. Nayak, S. Thota, D. Joshi, M. Krautz, A. Waske, A. Behler, J. Eckert, T. Sarkar, M. S. Andersson, R. Mathieu, *et al.*, Physical Review B **92**, 214434 (2015).
[30] P. Bag, P. Baral, and R. Nath, Physical Review B **98**, 144436 (2018).
[31] S. Ghosh, D. C. Joshi, P. Pramanik, S. K. Jena, S. Pittala, T. Sarkar, M. S. Seehra, and S. Thota, Journal of Physics: Condensed Matter **32**, 485806 (2020).
[32] C. Mulder, A. Van Duyneveldt, and J. Mydosh, Physical Review B **25**, 515 (1982).
[33] V. Singh, M. Seehra, and J. Bonevich, Journal of Applied Physics **105** (2009).
[34] S. Thota and M. Seehra, Journal of Applied Physics **113** (2013).
[35] P. Pramanik, R. Clulow, D. C. Joshi, A. Stolpe, P. Berastegui, M. Sahlberg, and R. Mathieu, Scientific Reports **14**, 3382 (2024).
[36] F. J. Dyson, Matematika **16**, 137 (1972).
[37] G. A. Baker Jr, Physical Review B **5**, 2622 (1972).
[38] O. M. Lefloch F., Hammann J. and V. E., Europhysics Letters **18**, 647 (1992).
[39] L. Dissado and R. Hill, Journal of Applied Physics **66**, 2511 (1989).
[40] A. Malinowski, V. Bezusyy, R. Minikayev, P. Dziawa, Y. Syryanyy, and M. Sawicki, Physical Review B **84**,

024409 (2011).
[41] S. Pakhira, C. Mazumdar, R. Ranganathan, S. Giri, and M. Avdeev, Physical Review B **94**, 104414 (2016).
[42] N. Khan, P. Mandal, and D. Prabhakaran, Physical Review B **90**, 024421 (2014).
[43] R. Chamberlin, G. Mozurkewich, and R. Orbach, Physical review letters **52**, 867 (1984).
[44] A. T. Ogielski, Physical Review B **32**, 7384 (1985).
[45] P. C. Hohenberg and B. I. Halperin, Reviews of Modern Physics **49**, 435 (1977).
[46] K. Weron, Journal of Physics: Condensed Matter **3**, 9151 (1991).
[47] R. Pickup, R. Cywinski, C. Pappas, B. Farago, and P. Fouquet, Physical review letters **102**, 097202 (2009).
[48] T. Naka, T. Nakane, S. Ishii, M. Nakayama, A. Ohmura, F. Ishikawa, A. De Visser, H. Abe, and T. Uchikoshi, Physical Review B **103**, 224408 (2021).
[49] J. N. Wagner, W. Häußler, O. Holderer, A. Bauer, S. M. Shapiro, and P. Böni, Quantum beam science **2**, 26 (2018).
[50] T. Naka, T. Nakane, J. Valenta, H. Mamiya, S. Ishii, M. Nakayama, H. Abe, T. Togashi, and T. Uchikoshi, Journal of Physics Communications **6**, 055001 (2022).
[51] C. Tsallis, *Introduction to nonextensive statistical mechanics: approaching a complex world*, Vol. 1 (Springer, 2009).
[52] R. Pickup, R. Cywinski, C. Pappas, B. Farago, and P. Fouquet, Physical review letters **102**, 097202 (2009).
[53] S. Pal, K. Kumar, A. Banerjee, S. Roy, and A. Nigam, Physical Review B **101**, 180402 (2020).
[54] R. Bhowmik and R. Ranganathan, Physical Review B **74**, 214417 (2006).
[55] D. Kumar, Journal of Physics: Condensed Matter **26**, 276001 (2014).
[56] B. C. Melot, J. E. Drewes, R. Seshadri, E. Stoudenmire, and A. P. Ramirez, Journal of Physics: Condensed Matter **21**, 216007 (2009).
[57] S. Thota, M. S. Seehra, M. R. Chowdhury, H. Singh, S. Ghosh, S. Jena, P. Pramanik, T. Sarkar, R. S. Rawat, R. Medwal, *et al.*, Physical Review B **106**, 134418 (2022).
[58] J. P. Palakkal, T. Faske, M. Major, I. Radulov, P. Komissinskiy, and L. Alff, Journal of Magnetism and Magnetic Materials **508**, 166873 (2020).
[59] M. Roy-Chowdhury, S. K. Jena, V. P. Khadse, D. C. Joshi, and S. Thota, Journal of Physics D: Applied Physics **56**, 355304 (2023).
[60] E. Yukhno, L. Bashkirov, L. Lobanovsky, S. Trukhanov, and S. Slonskaya, Inorganic Materials **52**, 218 (2016).
[61] C. Yu, X. Guan, G. Li, J. Zheng, and L. Li, Scripta Materialia **66**, 300 (2012).
[62] D. Ranaut, J. Kumar, and K. Mukherjee, Journal of Magnetism and Magnetic Materials **578**, 170833 (2023).
[63] K. K. Bharathi, R. Tackett, C. Botez, and C. Ramana, Journal of Applied Physics **109** (2011).
[64] N. Mottaghi, M. S. Seehra, J. Shi, M. Jain, and M. B. Holcomb, Journal of Applied Physics **128** (2020).
[65] J. R. de Almeida and D. J. Thouless, Journal of Physics A: Mathematical and General **11**, 983 (1978).
[66] M. Gabay and G. Toulouse, Physical Review Letters **47**, 201 (1981).
[67] B. Barbara, A. Malozemoff, and Y. Imry, Physical Review Letters **47**, 1852 (1981).
[68] A. Kumar, A. Senyshyn, and D. Pandey, Physical Review B **99**, 214425 (2019).
[69] Y. T. Wang, H. Y. Bai, M. X. Pan, W. H. Wang, *et al.*, Physical Review B **74**, 064422 (2006).
[70] S. Tiwari and K. Rajeev, Physical Review B **72**, 104433 (2005).
[71] M. K. Sharma and K. Mukherjee, Journal of Magnetism and Magnetic Materials **466**, 317 (2018).
[72] A. Singha, P. Pramanik, D. C. Joshi, S. Ghosh, S. Jena, P. Tiwari, T. Sarkar, and S. Thota, Journal of Physics: Condensed Matter **36**, 075802 (2023).
[73] P. Pramanik, S. Ghosh, P. Yanda, D. Joshi, S. Pittala, A. Sundaresan, P. Mishra, S. Thota, and M. Seehra, Physical Review B **99**, 134422 (2019).
[74] W. Akram, M. de h Óra, M. Bansal, R. Mukhopadhyay, J. MacManus-Driscoll, and T. Maity, Journal of Physics D: Applied Physics **57**, 055301 (2023).
[75] C. Kittel and P. McEuen, *Introduction to solid state physics* (John Wiley & Sons, 2018).
[76] E. Gopal, *Specific heats at low temperatures* (Springer Science & Business Media, 2012).
[77] J. Coey, S. Von Molnar, and R. Gambino, Solid State Communications **24**, 167 (1977).
[78] S. Banerjee, D. P. Panda, P. Yanda, and A. Sundaresan, Physical Review Materials **7**, 034405 (2023).